



Cite this: *RSC Adv.*, 2021, 11, 27681

# Ultralong NiSe nanowire anchored on graphene nanosheets for enhanced electrocatalytic performance of triiodide reduction†

Fengxia Yang, Meirui Mu and Keqiang Zhang \*

Like their higher-dimensional counterparts, nanowire structures possess desirable features for electrocatalysis applications. In this study, ultralong NiSe nanowires (of diameters 50–150 nm and length 20  $\mu\text{m}$ ) were successfully anchored onto graphene nanosheets (NiSe NW/RGO). The NiSe nanowires were coated with a thick ( $\sim 10$  nm) disordered surface replete with active sites. Benefiting from the fast charge-transfer channels and plentiful electroactive sites on the NiSe nanowires, in synergy with the high electroactive surface and electrical conductivity of the graphene nanosheets, the optimized NiSe NW/RGO exhibited a remarkably higher electrocatalytic activity than NiSe nanowires and typical Pt counter-electrodes (CEs). NiSe NW/RGO also exhibited the low charge-transfer resistance of  $1.64 \Omega \text{ cm}^2$  and delivered a higher power conversion efficiency (PCE = 7.99%) than Pt CEs (PCE = 7.76%).

Received 6th June 2021  
Accepted 10th August 2021

DOI: 10.1039/d1ra04367f

rsc.li/rsc-advances

## 1. Introduction

Dye-sensitized solar cells (DSSCs) have captured intensive scientific and technical interest as a potential candidate for next-generation solar cells.<sup>1–5</sup> Transition metal chalcogens can potentially replace the typically high-cost platinum (Pt) counter-electrode (CE) traditionally used in DSSCs, additionally, they may boost high power conversion efficiency of the cell.<sup>5–7</sup> Among these compounds, metal selenides have demonstrated superior electrocatalytic potential owing to their small electronegativity and intrinsic catalytic property.<sup>8–10</sup> Nickel-based selenides, with their unique electron states and intrinsic metallic properties, are especially acknowledged as potential electroactive materials in DSSC.<sup>11–14</sup> However, the crystal structure of nickel selenides naturally forms a spherical nanostructure, which encourages aggregation and reduces the number of exposed active sites for the electrocatalytic reaction, thereby lowering the reaction kinetics.

Active site exposure and fast reaction kinetics are essential for triggering the electrocatalytic process. For successful implantation, a high-performance electroactive material must possess a suitable microstructure and exhibit the correct physicochemical properties.<sup>15–17</sup> Pioneering works have suggested that constructing electroactive materials on the network structures of metals or carbon materials can significantly reduce the aggregation of electroactive materials while enhancing their reaction kinetics.<sup>18,19</sup> Among various carbon

materials, graphene nanosheets are ideal support that boost the electrical conductivity and catalytic activity of prospective catalysts.<sup>20–23</sup> Previously, we also proved that owing to their mesoporous structure and hollow-hybrid nanostructure, CEs composed of nickel selenides on graphene remarkably improve the electrocatalytic performance of DSSCs.<sup>24,25</sup>

Specific synthesis methods can engineer the thermodynamic and dynamic parameters during nucleation and growth of nanomaterials, breaking their customary nanostructures and dimensions. Such tailoring offers some unique advantages in electrocatalytic application.<sup>26,27</sup> Using a combined self-regulating acid etching and topotactic transformation strategy, Zheng *et al.* recently prepared vertically stacked ultrathin (1.25 nm thick) two-dimensional nonlayered nanosheets of nickel selenide.<sup>28</sup> Even more intriguingly, Yu *et al.* synthesized ultrathin one-dimensional Fe-doped NiSe<sub>2</sub> nanowires (of diameter 1.7 nm) by a colloidal technique mediated by a soft template, which demonstrated efficient electrocatalytic performance.<sup>29</sup> The disordered surface layers on the nanowires provided abundant active sites for the electrocatalytic reaction, and the nanowire structure enhanced the diffusion of electrolyte molecules. These features are highly promising for electrocatalysis applications.<sup>30,31</sup>

In this work, we report a rational and facile approach for anchoring NiSe nanowires (NW) on graphene (RGO). The resulting structure, designated NiSe NW/RGO, is a highly efficient electroactive material for DSSCs. Its intrinsic properties, such as unsaturated edge sites, abundant charge-transfer, numerous electrolyte-transmission channels and high electroactive surface area, improve the collection, transfer, and utilization of photo-generated electrons. Accordingly, the catalytic activity of triiodide reduction is much higher on NiSe NW/RGO than on NiSe NW and Pt. In particular, the power conversion of

Agro-Environmental Protection Institute, Ministry of Agriculture and Rural Affairs, Tianjin 300191, China. E-mail: keqiangzhang68@163.com

† Electronic supplementary information (ESI) available. See DOI: 10.1039/d1ra04367f



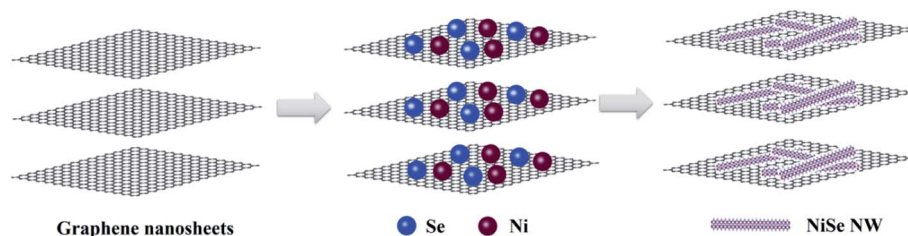


Fig. 1 Schematic diagram of the synthesis process of NiSe nanowire anchored on the surface of graphene nanosheets.

the DSSC device fabricated with the NiSe NW/RGO CE (PCE = 7.99%) exceeded that of a DSSC with a Pt CE (PCE = 7.76%).

## 2. Experimental section

### 2.1 Synthesis of NiSe NW/RGO and NiSe NW

Graphene oxide (GO) nanosheets were prepared by a modified Hummers method.<sup>32</sup> The NiSe NW/RGO and NiSe NW were fabricated by a modified strategy developed by Li *et al.* and our group.<sup>24,33</sup> In detail, as shown in Fig. 1, 0.5 mmol of  $\text{NiSO}_4 \cdot 7\text{H}_2\text{O}$  and 5 mL of GO water suspension ( $10 \text{ mg mL}^{-1}$ ) were dissolved in 30 mL of deionized water in a 50 mL Teflon-lined autoclave. Next, 1.0 g of a chelating agent (ethylenediaminetetraacetic acid) and 0.1 g of a template (polyvinylpyrrolidone, mol. wt. 40 000) were added to the above solution, along with 1.0 g of NaOH to maintain the pH at  $\sim 14$ . After one hour of continuous stirring, a selenium source (1.5 mmol of  $\text{Na}_2\text{SeO}_3 \cdot 5\text{H}_2\text{O}$ ) was

added to the mixture. Finally, 5 mL of hydrazine hydrate was added to reduce the  $\text{Na}_2\text{SeO}_3$  and GO. This mixture was stirred for 5 minutes, then sealed in the autoclave and heated at  $180^\circ\text{C}$  for 15 h. After naturally cooling the autoclave to room temperature, the NiSe NW/RGO product was removed, washed with water and absolute ethanol to remove any impurities, and then dried at  $60^\circ\text{C}$ . NiSe NW samples were obtained under the same reaction conditions but without adding GO.

### 2.2 Characterization of the obtained electrocatalysts

The crystallinity and composition of the samples were characterized by X-ray diffraction (XRD, D/max-2500, Japan Science) with Cu K $\alpha$  radiation ( $\lambda = 1.54056 \text{ \AA}$ ). The sample morphologies were studied by field-emission scanning electron microscopy (FE-SEM, Zeiss Merlin Compact) equipped with energy dispersive spectroscopy (EDS) mapping for measuring the elements in the samples. The microstructures of the samples were clarified

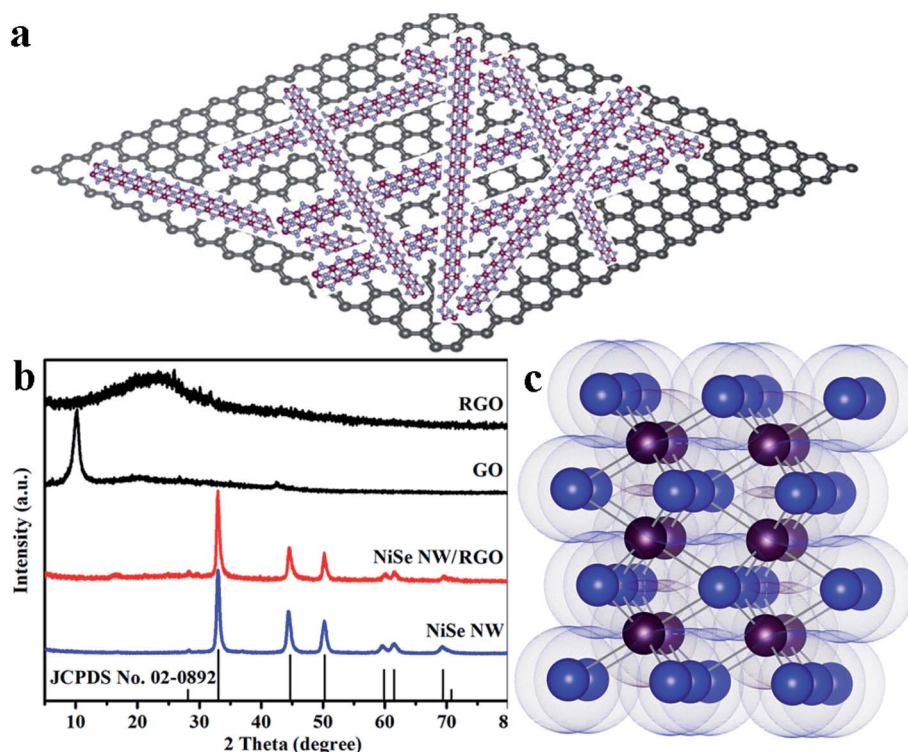


Fig. 2 Schematic diagram of NiSe nanowires anchored on graphene nanosheets (a). XRD patterns (b) of NiSe NW, NiSe NW/RGO, GO and RGO. Crystal structure (c) of hexagonal NiSe (Ni purple, Se blue).



by high-resolution transmission electron microscopy (HR-TEM, Tecnai G2 F20) operated at 200 kV (FEI). The chemical compositions of the samples were then analyzed by X-ray photoelectron spectroscopy (XPS). The obtained materials were applied as the CE of DSSCs to characterize their electrocatalytic performances. The electrochemical measurements and CE characterizations of the CEs and DSSCs are detailed in the ESI.†

### 3. Results and discussion

The schematic diagram of NiSe nanowires anchored on graphene nanosheets is illustrated in Fig. 2a. The crystallite structures and purity of the resulting NiSe NW, NiSe NW/RGO, GO and RGO were analyzed by X-ray diffraction (XRD). As shown in Fig. 2b, the sharp peak at  $10.02^\circ$  in the GO spectrum was ascribed to water molecules and various oxygen-containing groups (hydroxyl, epoxy, and carboxyl groups) acquired during the oxidation process of graphite.<sup>34,35</sup> After further solvothermal reaction, the GO was reduced to RGO, and the sharp peak of GO was replaced with the broad peak of RGO at approximately  $15\text{--}30^\circ$ . All diffraction peaks of NiSe NW/RGO and NiSe NW in the XRD patterns both can be indexed to the nickel selenide (JCPDS no. 02-0892). The well-defined peaks at  $27.9^\circ$ ,  $32.8^\circ$ ,  $44.4^\circ$ ,  $49.9^\circ$  and  $59.6^\circ$  corresponded to nickel selenide (100), (101), (102), (110) and (103), respectively. No characteristic peak of other phases such as  $\text{Ni}_{0.85}\text{Se}$  or  $\text{Ni}_3\text{Se}_4$  were observed. The lack of any obvious RGO peak in the XRD pattern of NiSe NW/RGO was attributed to the low RGO content in the nanocomposites.

The chemical states and elemental compositions of the NiSe NW/RGO samples were further investigated by X-ray

photoelectron spectroscopy (XPS). As shown in Fig. 3a, two sets of typical 2p peaks of the  $\text{Ni}^{2+}$  oxidation state could be observed at 855.8 (Ni 2p<sub>3/2</sub>) and 873.6 eV (Ni 2p<sub>1/2</sub>), with two shakeup satellites appearing at 861.4 and 880.2 eV.<sup>36</sup> The two Se 3d peaks in Fig. 3b, centered at 54.2 and 55.2 eV respectively, correspond to Se 3d<sub>5/2</sub> and 3d<sub>3/2</sub>, while the peak at 58.8 eV could be assigned to surface oxidation of the Se species.<sup>37</sup> The XPS peaks of Ni 2p and Se 3d were consistent with the corresponding binding energies of NiSe, demonstrating the successful synthesis of NiSe. Fig. 3c and S1† are typical SEM images of NiSe NW/RGO. The graphene nanosheets wrapped around the surfaces of numerous NiSe NW formed the favorable nest-like structures of NiSe NW/RGO. Furthermore, whereas the NiSe NWs were slightly aggregated in their pure state (Fig. S2†), they were monodispersed on the NiSe NW/RGO. Their length (approximately 20  $\mu\text{m}$ ) also increased the specific surface area of the structure. Under higher SEM magnification, the diameter of the NiSe nanowires was revealed as 50–150 nm (Fig. 3d).

The TEM images (Fig. 4a and S3†) confirmed that the NiSe nanowires were dispersed on the surface of graphene nanosheets. Moreover, the HR-TEM image (Fig. 4b) revealed that NiSe nanowires have an approximately 10 nm-thick disordered surfaces, which provided plenty of defects favoring the electrocatalytic performance.<sup>38</sup> The lattice fringe spacings of approximately 0.27 and 0.24 nm in the HR-TEM image (Fig. 4c) were indexed to the (101) and (102) crystal planes of the NiSe phase, respectively. The EDS elemental mapping (Fig. 4d–f) reveals that the Ni and Se elements were uniformly distributed through single nanowires. The EDS profiles indicate the existence of C, Ni, Se (Fig. 4f). The C peak was contributed by

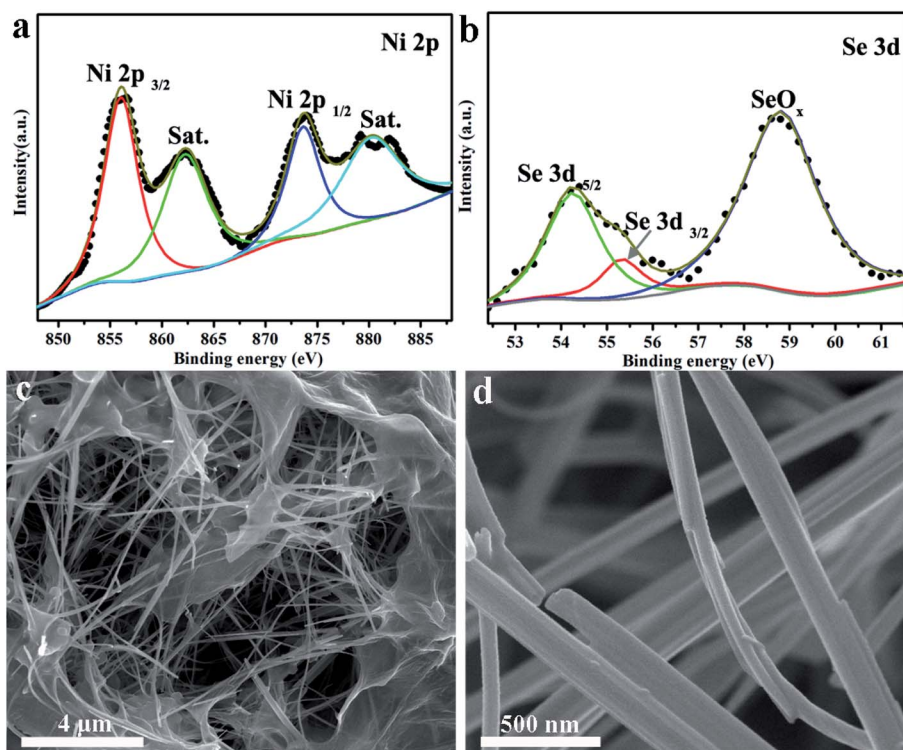


Fig. 3 XPS analysis of the Ni 2p (a) and Se 3d (b) spectra of NiSe NW/RGO. Different magnified SEM images (c and d) of NiSe NW/RGO.



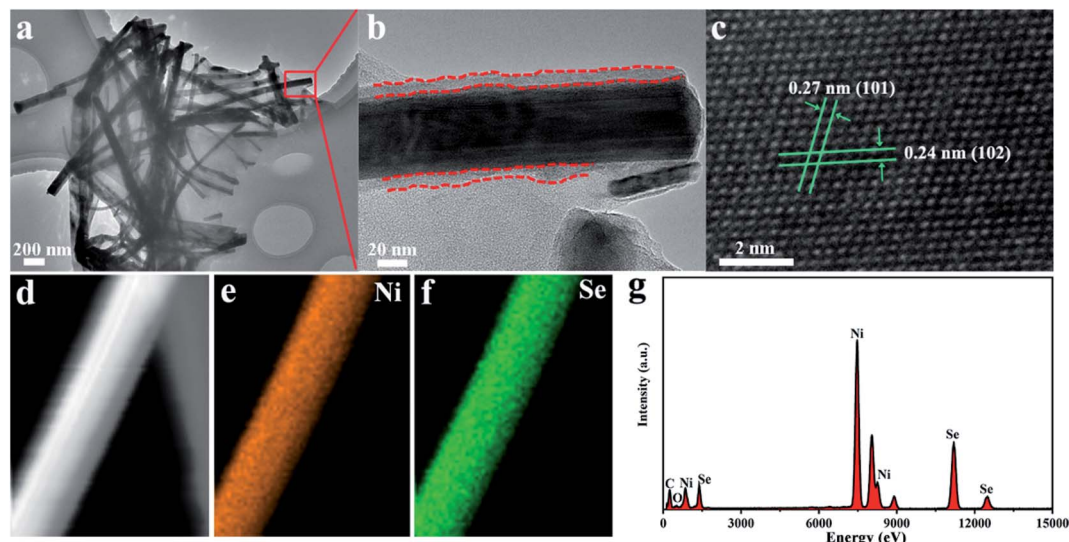


Fig. 4 TEM and HRTEM images (a–c) of NiSe NW/RGO. EDS elemental mapping images (d–f) and corresponding EDS profiles (g) of NiSe NW/RGO.

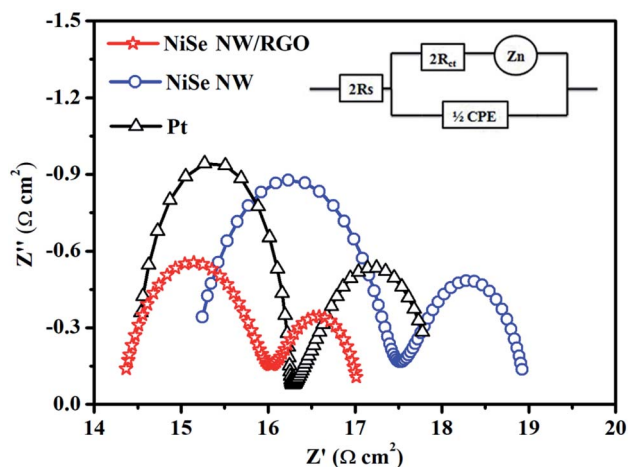


Fig. 5 Nyquist plots for dummy cells fabricated with NiSe NW/RGO, NiSe NW and Pt CEs.

graphene, whereas the Ni and Se peaks arose from the NiSe NW products. The molar ratio of the Ni and Se elements in the EDS pattern was nearly 1 : 1.

The electron-transport property at the electrode–electrolyte interface is crucial for evaluating the electrocatalytic performance of CE materials. For this purpose, symmetric cells (CE/

electrolyte/CE) was constructed and subjected to electrochemical impedance spectroscopy (EIS). Fig. 5 presents the Nyquist plots of NiSe NW/RGO, NiSe NW and Pt CEs. The series resistance ( $R_s$ ), charge-transfer resistance ( $R_{ct}$ ), Nernst diffusion impedance ( $Z_w$ ) and the corresponding constant phase element (CPE) can be obtained from the high-frequency to low-frequency semicircle.<sup>39,40</sup> All EIS spectra were fitted by an equivalent circuit model using Z-view software (Fig. 5, inset), and the obtained EIS parameters are shown in Table 1.  $R_s$  is inversely related to ohmic contact and bonding strength between the fluorine-doped tin oxide substrate and CE film, whereas  $R_{ct}$  was negatively correlated with the charge-transfer kinetics of  $I_3^-$  reduction. The lower  $R_s$  of NiSe NW/RGO than NiSe NW and Pt CEs (Table 1) confirmed that the two-dimensional conductive network of graphene enhanced the electron shuttle from the external circuit to NiSe NW.<sup>20</sup> The  $R_{ct}$  of NiSe NW was  $2.31 \Omega \text{ cm}^2$ , but that of NiSe NW/RGO (with the NiSe NW grown on graphene) was only  $1.64 \Omega \text{ cm}^2$ , lower than that of Pt CE ( $R_{ct} = 1.79 \Omega \text{ cm}^2$ ). The small  $R_{ct}$  of NiSe NW/RGO indicates that the combined NiSe NW and RGO decreased the electron-transport resistance and improved the charge-transfer ability at the electrode–electrolyte interface. Notably, the NiSe NW/RGO achieved lower  $Z_w$  and larger CPE than other CEs, further demonstrating its superior electrocatalytic performance. These favorable charge transfer and ion diffusion properties could enhance the reaction

Table 1 Detailed parameters of electrochemical impedance spectroscopy spectra<sup>a</sup>

CEs	$R_s (\Omega \text{ cm}^2)$	$R_{ct} (\Omega \text{ cm}^2)$	$Z_w (\Omega \text{ cm}^2)$	CPE (F)	$\tau$ (s)
NiSe NW/RGO	14.29	1.64	1.14	$2.90 \times 10^{-4}$	$1.90 \times 10^{-3}$
NiSe NW	15.08	2.31	1.59	$5.06 \times 10^{-5}$	$4.68 \times 10^{-4}$
Pt	14.46	1.79	1.74	$7.03 \times 10^{-5}$	$5.05 \times 10^{-4}$

<sup>a</sup> Electron lifetime was expressed as  $\tau = R_{ct} \times \text{CPE}/S$ , where  $S$  is the area of CEs ( $0.25 \text{ cm}^2$ ).



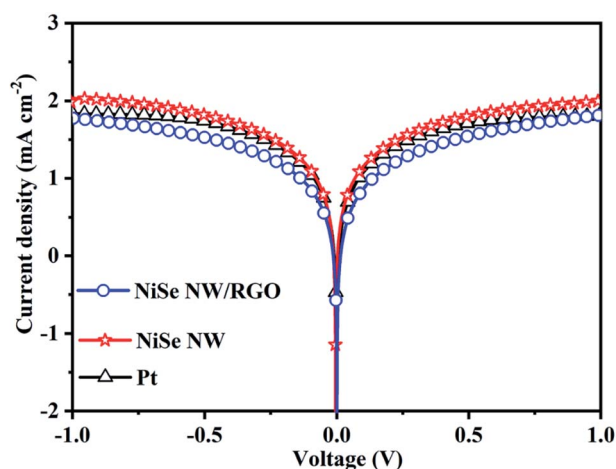


Fig. 6 Tafel polarization curves of the symmetrical cells based on NiSe NW/RGO, NiSe NW and Pt CEs.

kinetics of triiodide reduction, admitting a larger amount of charge through the electrode/electrolyte interface.<sup>41,42</sup>

The catalytic and diffusion properties of the prepared CEs were investigated by Tafel polarization (Fig. 6). The specimens in this experiment were the symmetrical dummy electrodes used in the EIS experiment. The exchange current density ( $J_0$ ) can be obtained from the intercepts of the linear fits to the cathodic and anodic polarization curves (Fig. S5†). Meanwhile, the limiting diffusion current density ( $J_{lim}$ ) can be obtained from the y-intercept of the cathodic branch.<sup>43,44</sup> The obtained  $J_0$  and  $J_{lim}$  values are summarized in Table 1. The NiSe NW/RGO

yielded a higher  $J_0$  ( $0.80 \text{ mA cm}^{-2}$ ) than NiSe NW ( $0.54 \text{ mA cm}^{-2}$ ) and Pt ( $0.69 \text{ mA cm}^{-2}$ ) CEs, revealing that the intrinsic electron-transfer ability was higher in NiSe NW/RGO than in the other CE. Similarly, the  $J_{lim}$  values decreased in the order NiSe NW/RGO ( $2.05 \text{ mA cm}^{-2}$ ) > Pt ( $1.84 \text{ mA cm}^{-2}$ ) > NiSe NW ( $1.80 \text{ mA cm}^{-2}$ ), suggesting the best diffusion property of NiSe NW/RGO.<sup>45</sup> In summary, the Tafel polarization measurements further indicate the superior electrocatalytic property of NiSe NW/RGO, therefore NiSe NW/RGO is expected to achieve high photovoltaic performance.

The reaction kinetics and catalytic activities of the as-prepared CE materials were determined by cyclic

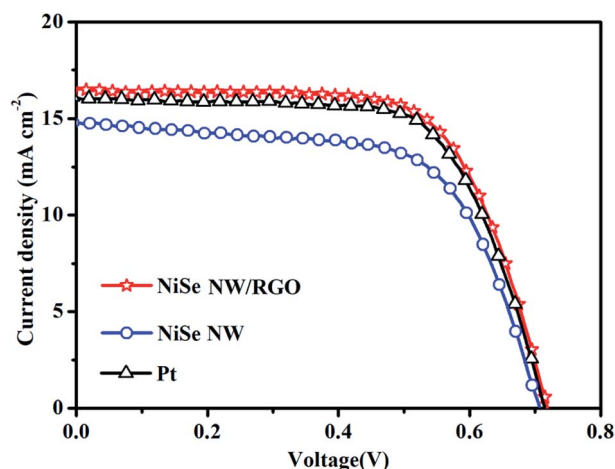


Fig. 8 Photocurrent density–voltage curves of devices based on NiSe NW/RGO, NiSe NW and Pt CEs.

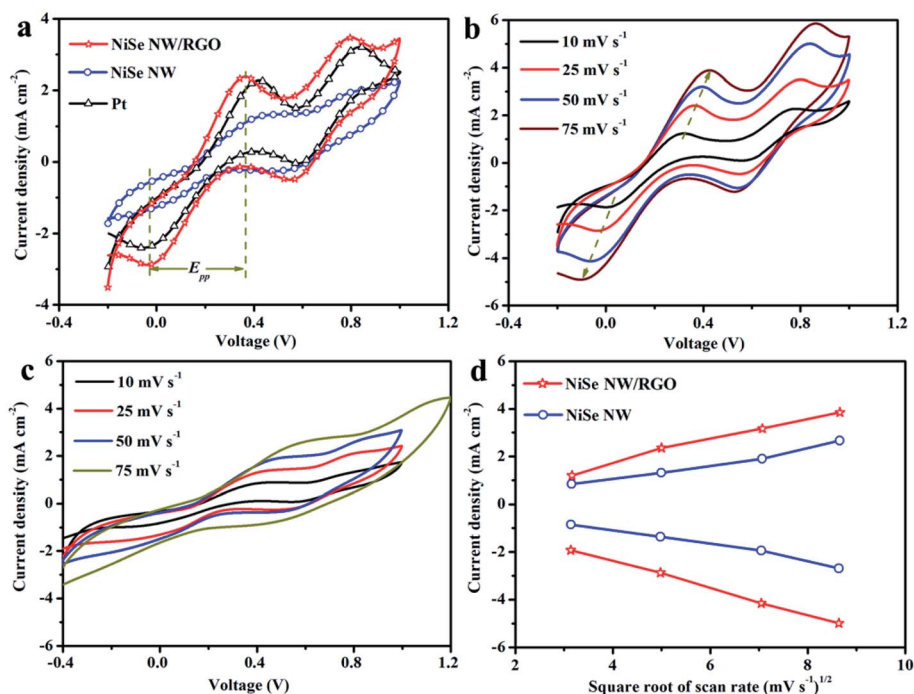


Fig. 7 Cyclic voltammograms (a) of the NiSe NW/RGO, NiSe NW and Pt CEs at a scan rate of  $25 \text{ mV s}^{-1}$ . Cyclic voltammograms of NiSe NW/RGO (b) and NiSe NW (c) at different scan rates. Relationship between redox current densities and the square root of the scan rates (d).



Table 2 Electrocatalytic parameters derived from Tafel, CV and  $J$ - $V$  curves of DSSCs based on different CEs

CEs	$J_{SC}$ (mA cm <sup>-2</sup> )	$V_{OC}$ (V)	FF (%)	PCE (%)	$J_{lim}$ (mA cm <sup>-2</sup> )	$J_0$ (mA cm <sup>-2</sup> )	$E_{pp}$ (mV)	$J_{Ox-1}$ (mA cm <sup>-2</sup> )
NiSe NW/RGO	16.45	0.72	67.46	7.99	2.05	0.80	395	2.38
NiSe NW	14.70	0.71	63.91	6.76	1.80	0.54	471	1.32
Pt	16.06	0.72	67.11	7.76	1.84	0.69	432	2.28

voltammetry (CV) in a three-electrode system at a scan rate of 25 mV s<sup>-1</sup>. Fig. 7 clarifies two typical pairs of prominent redox peaks (Oxd-1/Red-1 and Oxd-2/Red-2). The negative (left side) and positive (right side) pairs respectively correspond to eqn (1) and (2):



Besides collecting electrons from external circuit, CEs play vital roles in the  $I_3^-$  to  $I^-$  reduction. The current intensity of the cathodic peak ( $J_{Ox-1}/J_{Red-1}$ ) and peak-to-peak separation ( $E_{pp}$ ) between the anodic and cathodic peaks of the negative pair are well-used indices of the electrocatalytic performance of CEs. With its expanded catalytic surface area, the graphene increases the number of efficient transfer channels for electrons and electrolytes in NiSe NW/RGO. Accordingly, the NiSe NW/RGO CE achieved a higher current density and faster  $I_3^-$  reduction rate than NiSe NW and Pt CEs. These results are consistent with the  $J_{Ox-1}$ , which decreased in the order NiSe NW/RGO (2.38 mA cm<sup>-2</sup>) > Pt (2.28 mA cm<sup>-2</sup>) > NiSe NW (1.32 mA cm<sup>-2</sup>). The enhanced electrocatalytic activity of NiSe nanowire on graphene was also reflected in the lower  $E_{pp}$  of NiSe NW/RGO than the other CEs. The  $E_{pp}$  is usually inversely correlated with the typical electrochemical rate constant of the redox-reaction kinetics, and is positively correlated with overpotential loss.<sup>46</sup> The higher

$J_{Ox-1}$  and lower  $E_{pp}$  imply that the connection between NiSe nanowire and graphene not only sufficiently drove ion diffusion and accelerated electron transfer, but also favored the electrocatalytic activity toward the  $I^-/I_3^-$  redox reaction, thereby increasing the photocurrent density and fill factor of the DSSC.<sup>47</sup> Meanwhile, the CV responses (Fig. 7b and c) of NiSe NW/RGO and NiSe NW at different scan rates ranging from 10 to 75 mV s<sup>-1</sup> were also measured. Both the peak current densities and  $E_{pp}$  of NiSe NW/RGO and NiSe NW increased with scan rate, as listed in Table S1.† Additionally, the Ox-1/Red-1 peak current densities of NiSe NW/RGO and NiSe NW exhibited a good linear relationship (Fig. 7d) with the square root of the scan rate, indicating that their electrocatalytic behavior on the electrode surface depended on a diffusion-controlled mechanism.

The photovoltaic performances of the DSSCs installed with NiSe NW/RGO, NiSe NW and Pt CEs were measured under simulated sunlight with an intensity of 100 mW cm<sup>-2</sup>. The photocurrent-voltage curves of the three CEs are shown in Fig. 8 and S6,† and the corresponding photovoltaic parameters are summarized in Table 2. The NiSe NW/RGO exhibited a much higher photovoltaic property than the NiSe NW electrode, as evidenced by its higher short-current density ( $J_{SC}$ ), fill factor (FF) and power conversion efficiency (PCE). The NiSe NW structure provided fast charge-transfer channels and numerous electroactive sites, conferring an intrinsically efficient electrocatalytic activity. Meanwhile, the RGO support improved the

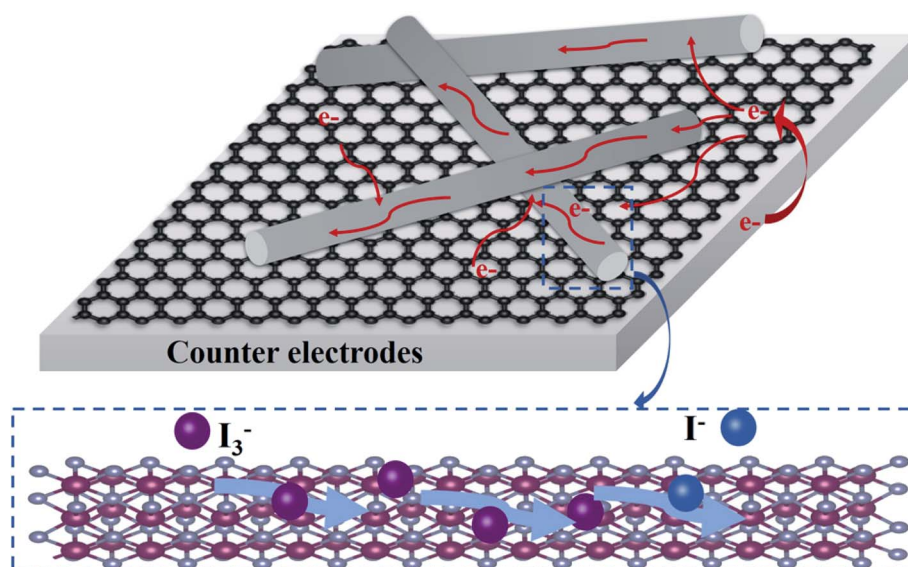


Fig. 9 Schematic diagram of charge-transfer process and electrocatalytic reaction of NiSe NW/RGO as CE.





electroactive surface, accelerating the transfer of electrons and electrolytes, and enhancing the availability of electrocatalytic active sites. These phenomena explain the superior EIS, CV and Tafel polarization performances of NiSe NW/RGO.<sup>48</sup> The advanced properties of NiSe NW/RGO ensure the excellent collection, transfer, and utilization of photo-generated electrons in this material, and a high catalytic activity for  $\text{I}_3^-$  reduction. Therefore, the  $J_{\text{SC}}$  ( $16.45 \text{ mA cm}^{-2}$ ) and FF (67.46%) of NiSe NW/RGO exceeded those of the Pt CE ( $J_{\text{SC}} = 16.06 \text{ mA cm}^{-2}$ , PCE = 67.11%). The PCE of DSSC device with NiSe NW/RGO CE was 7.99%, versus 7.76% in the device with Pt CE (Fig. 9).

## 4. Conclusions

Ultralong NiSe nanowires were successfully anchored onto graphene nanosheets. This specific composite nanostructure exhibited excellent intrinsic properties, such as unsaturated edge sites, abundant charge-transfer, numerous electrolyte-transmission channels, and an improved electroactive surface. The electrocatalytic performance of NiSe NW/RGO was systematically characterized by EIS, Tafel polarization, and CV. The possible electrocatalysis effect of NiSe NW/RGO on triiodide reduction was then proposed. DSSC devices based on the NiSe NW/RGO electrode achieved a power conversion efficiency of 7.99%, obviously higher than that of single NiSe NW, and even superior to that of a Pt electrode. It was concluded that the NiSe nanowire/graphene nanostructures are effective tools for exploring high-performance electroactive materials in DSSCs.

## Conflicts of interest

There are no conflicts to declare.

## Acknowledgements

This work was funded by National Science Foundation of China (41807399, 42077355) and Fundamental Cutting-edge Projects of Research Institute (2021-jcqrw-yfx).

## References

- 1 M. G. Brian O'Regan, *Nature*, 1991, **353**, 737–740.
- 2 A. Yella, H. W. Lee, H. N. Tsao, C. Y. Yi, A. K. Chandiran, M. K. Nazeeruddin, E. W. G. Diau, C. Y. Yeh, S. M. Zakeeruddin and M. Gratzel, *Science*, 2011, **334**, 629–634.
- 3 M. Freitag, J. Teuscher, Y. Saygili, X. Zhang, F. Giordano, P. Liska, J. Hua, S. M. Zakeeruddin, J. E. Moser, M. Gratzel and A. Hagfeldt, *Nat. Photonics*, 2017, **11**, 372–378.
- 4 J. X. Yao, X. Q. Zuo, W. Wang, Y. K. Zhang, Q. Yang, H. B. Tang, S. W. Jin, S. M. Chen, Y. X. Lin and G. Li, *Chem. Eng. J.*, 2021, **407**, 127205.
- 5 M. Kokkonen, P. Talebi, J. Zhou, S. Asgari, S. A. Soomro, F. Elsehrawy, J. Halme, S. Ahmad, A. Hagfeldt and S. G. Hashmi, *J. Mater. Chem. A*, 2021, **9**, 10527–10545.
- 6 J. Wu, Z. Lan, J. Lin, M. Huang, Y. Huang, L. Fan, G. Luo, Y. Lin, Y. Xie and Y. Wei, *Chem. Soc. Rev.*, 2017, **46**, 5975–6023.
- 7 Q. Miao, Y. Du, G. Wang, Z. Sun, Y. Zhao and S. Zhang, *J. Mater. Chem. A*, 2019, **7**, 5967–5980.
- 8 Z. T. Jin, M. R. Zhang, M. Wang, C. Q. Feng and Z. S. Wang, *Acc. Chem. Res.*, 2017, **50**, 895–904.
- 9 S. L. Jian, Y. J. Huang, M. H. Yeh and K. C. Ho, *J. Mater. Chem. A*, 2018, **6**, 5107–5118.
- 10 Y. Y. Duan, Q. W. Tang, J. Liu, B. L. He and L. M. Yu, *Angew. Chem., Int. Ed.*, 2014, **53**, 14569–14574.
- 11 X. Wang, Y. Xie, K. Pan, J. Wu, Y. Xiao, P. Yu, W. Zhou and H. Fu, *ACS Appl. Nano Mater.*, 2018, **1**, 4900–4909.
- 12 W. J. Hou, Y. M. Xiao and G. Y. Han, *Angew. Chem., Int. Ed.*, 2017, **56**, 9146–9150.
- 13 Y. Q. Jiang, X. Qian, C. L. Zhu, H. Y. Liu and L. X. Hou, *ACS Appl. Nano Mater.*, 2018, **10**, 9379–9389.
- 14 P. K. Wei, Z. W. Hao, Y. Yang and L. Liu, *Appl. Surf. Sci.*, 2021, **553**, 149567.
- 15 C. Gu, S. J. Hu, X. S. Zheng, M. R. Gao, Y. R. Zheng, L. Shi, Q. Gao, X. Zheng, W. S. Chu, H. B. Yao, J. F. Zhu and S. H. Yu, *Angew. Chem., Int. Ed.*, 2018, **57**, 4020–4024.
- 16 H. J. Zhang, X. T. Li, X. F. Meng, S. T. Zhou, G. Yang and X. M. Zhou, *J. Phys.: Condens. Matter*, 2019, **31**, 125301.
- 17 N. N. Li, C. Zhu, J. W. Zhang, H. Y. Jing, J. W. Hu, C. Hao and Y. T. Shi, *Chem. Commun.*, 2021, **57**, 5302–5305.
- 18 Q. Q. Miao, Y. Y. Du, G. T. Wang, Z. C. Sun, Y. H. Zhao and S. J. Zhang, *J. Mater. Chem. A*, 2019, **7**, 5967–5980.
- 19 W. Wei, D. Stacchiola, N. Akter, J. A. Boscoboinik and Y. H. Hu, *ACS Appl. Energy Mater.*, 2019, **2**, 1445–1451.
- 20 V. Murugadoss, N. Wang, S. Tadakamalla, B. Wang, Z. H. Guo and S. Angaiah, *J. Mater. Chem. A*, 2017, **5**, 14583–14594.
- 21 W. Yang, Z. H. Li, X. W. Xu, L. Q. Hou, Y. S. Tang, B. J. Deng, F. Yang, Y. Wang and Y. F. Li, *Chem. Eng. J.*, 2018, **349**, 782–790.
- 22 J. Y. Xi, R. Jia, W. Li, J. Wang, F. Q. Bai, R. I. Eglitis and H. X. Zhang, *J. Mater. Chem. A*, 2019, **7**, 2730–2740.
- 23 C. Tamilselvi, P. Duraisamy and N. Subathra, *Diamond Relat. Mater.*, 2021, **116**, 108396.
- 24 X. Zhang, Y. X. Yang, S. Q. Guo, F. Z. Hu and L. Liu, *ACS Appl. Nano Mater.*, 2015, **7**, 8457–8464.
- 25 X. Zhang, M. M. Zhen, J. W. Bai, S. W. Jin and L. Lie, *ACS Appl. Nano Mater.*, 2016, **8**, 17187–17193.
- 26 J. Q. Xu, X. D. Li, Z. Y. Ju, Y. F. Sun, X. C. Jiao, J. Wu, C. M. Wang, W. S. Yan, H. X. Ju, J. F. Zhu and Y. Xie, *Angew. Chem., Int. Ed.*, 2019, **58**, 3032–3036.
- 27 X. F. Lu, L. Yu and X. W. Lou, *Sci. Adv.*, 2019, **5**, 6009.
- 28 H. Wu, X. Lu, G. Zheng and G. W. Ho, *Adv. Energy Mater.*, 2018, **8**, 1702704.
- 29 C. Gu, S. Hu, X. Zheng, M. R. Gao, Y. R. Zheng, L. Shi, Q. Gao, X. Zheng, W. Chu, H. B. Yao, J. Zhu and S. H. Yu, *Angew. Chem.*, 2018, **57**, 4020–4024.
- 30 K. S. Yu, X. L. Pan, G. B. Zhang, X. B. Liao, X. B. Zhou, M. Y. Yan, L. Xu and L. Q. Mai, *Adv. Energy Mater.*, 2018, **8**, 1802369.

- 31 L. Q. Mai, J. Z. Sheng, L. Xu, S. S. Tan and J. S. Meng, *Acc. Chem. Res.*, 2018, **51**, 950–959.
- 32 X. Zhang, S. Q. Guo, M. M. Zhen, G. D. Gao and L. Liu, *J. Electrochem. Soc.*, 2015, **162**, H774–H779.
- 33 Z. B. Zhuang, Q. Peng, J. Zhuang, X. Wang and Y. D. Li, *Chem.–Eur. J.*, 2006, **12**, 211–217.
- 34 T. F. Yeh, J. M. Syu, C. Cheng, T. H. Chang and H. S. Teng, *Adv. Funct. Mater.*, 2010, **20**, 2255–2262.
- 35 Z. J. Fan, K. Wang, T. Wei, J. Yan, L. P. Song and B. Shao, *Carbon*, 2010, **48**, 1686–1689.
- 36 S. C. Chen, Z. X. Kang, X. Hu, X. D. Zhang, H. Wang, J. F. Xie, X. S. Zheng, W. S. Yan, B. C. Pan and Y. Xie, *Adv. Mater.*, 2017, **29**, 1701687.
- 37 Z. D. Huang, J. H. Liu, Z. Y. Xiao, H. Fu, W. D. Fan, B. Xu, B. Dong, D. Liu, F. N. Dai and D. F. Sun, *Nanoscale*, 2018, **10**, 22758–22765.
- 38 Z.-H. Huang, F.-F. Sun, M. Batmunkh, W.-H. Li, H. Li, Y. Sun, Q. Zhao, X. Liu and T.-Y. Ma, *J. Mater. Chem. A*, 2019, **7**, 11826–11835.
- 39 J. X. Yao, K. Zhang, W. Wang, X. Q. Zuo, Q. Yang, H. B. Tang, M. Z. Wu and G. Li, *Nanoscale*, 2018, **10**, 7946–7956.
- 40 W. Wang, J. Yao, X. Zuo, Q. Yang, M. Wu, H. Tang, S. Jin and G. Li, *Nanoscale Horiz.*, 2019, **4**, 1211–1220.
- 41 C. T. Li, C. P. Lee, I. T. Chiu, R. Vittal, Y. J. Huang, T. Y. Chen, H. W. Pang, J. T. Lin and K. C. Ho, *J. Mater. Chem. A*, 2017, **5**, 14079–14091.
- 42 K. Z. Wu, P. Y. Fu, B. Ruan, M. M. Wu, M. X. Wu and R. T. Wu, *New J. Chem.*, 2021, **45**, 1686–1694.
- 43 J. X. Yao, K. Zhang, W. Wang, X. Q. Zuo, Q. Yang, H. B. Tang, M. Z. Wu and G. Li, *ACS Appl. Nano Mater.*, 2018, **10**, 19564–19572.
- 44 U. Mehmood, A. Ishfaq and M. Sufyan, *Sol. Energy*, 2021, **220**, 949–952.
- 45 F. Du, X. Q. Zuo, Q. Yang, G. Li, Z. L. Ding, M. Z. Wu, Y. Q. Ma and K. R. Zhu, *J. Mater. Chem. C*, 2016, **4**, 10323–10328.
- 46 Y. C. Wang, D. Y. Wang, Y. T. Jiang, H. A. Chen, C. C. Chen, K. C. Ho, H. L. Chou and C. W. Chen, *Angew. Chem., Int. Ed.*, 2013, **52**, 6694–6698.
- 47 C. Xu, Y. Jiang, J. Yang, W. Wu, X. Qian and L. Hou, *Chem. Eng. J.*, 2018, **343**, 86–94.
- 48 T. Liu, X. Mai, H. Chen, J. Ren, Z. Liu, Y. Li, L. Gao, N. Wang, J. Zhang, H. He and Z. Guo, *Nanoscale*, 2018, **10**, 4194–4201.

